Springer

Journal of
Mechanical
Science and
Technology

Journal of Mechanical Science and Technology 22 (2008) 2286~2298

www.springerlink.com/content/1738-494x
DOI 10.1007/s12206-008-0618-z

Unsteady viscous flows past blunt bodies at moderate Reynolds numbers †

Moon-Sang Kim*, Hae-Moon Jeon and Yeong-Taek Lim

School of Aerospace and Mechanical Engineering, Korea Aerospace University, Kyungki-Do, 412-791, Korea

(Manuscript Received February 18, 2008; Revised June 25, 2008; Accepted June 25, 2008)

Abstract

Unsteady viscous flows past blunt bodies are simulated at the Reynolds numbers of 100, 200, 300, and 400. This research focuses on understanding the effects of the Reynolds numbers and blunt body shapes on the unsteady lift and drag forces. The incompressible Navier-Stokes flow solver, which employs the SIMPLER method in the two-dimensional body-intrinsic orthogonal curvilinear coordinate system, is verified by comparing the present numerical results with currently available experimental and numerical data. In conclusion, it is observed that the body shapes and the Reynolds numbers affect significantly the frequencies of the force oscillations as well as the mean values and the amplitudes of the drag and lift force oscillations.

Keywords: Unsteady flow; Blunt bodies; Vortex shedding; Incompressible flow; Drag and lift

1. Introduction

The analysis of flow field around blunt bodies has been carried out continuously with a great deal of attention because of its engineering significance. A near wake flow region behind a blunt body has alternating vortex shedding, and this vortex shedding leads to periodically oscillating drag and lift forces. Especially the oscillating lift force, whose direction is transverse to the flow, is large and may cause structural vibrations, acoustic noise generation, or resonance that may yield structural destructions, for example, the Tacoma Narrows suspension bridge disaster. Since the bridge collapsed due to wind-induced large-amplitude vibrations on November 7, 1940, many researchers have studied unsteady flows past blunt bodies.

Understanding of vortex shedding characteristics is very important for safe and efficient design of engineering structures such as flying wires, ocean pipelines, road vehicles, high towers, suspension bridges, skyscrapers, and high-speed trains, etc.

For the first time, many studies have accomplished the flows around circular cylinders because of its geometric simplicity. The periodicity of the wake of a blunt body is associated with the formation of a stable street of staggered vortices by von Kármán[1]. In his paper, he analyzed the stability of vortex street configurations and established a theoretical link between the vortex street structure and the drag on the body. Jordan and Fromm[2] investigated oscillatory drag, lift, and torque on a circular cylinder in a uniform flow at Reynolds numbers of 100, 400, and 1,000 by solving vorticity-stream function formulation. They showed the dramatic rise of the drag coefficient during the development of the Kármán vortex street. A detailed study of the wake structures and flow dynamics associated with simulated two-dimensional flows past a circular cylinder that is either stationary or in simple harmonic cross-flow oscillation was done by Blackburn and Henderson[3]. Manzari[4] presented a finite element solution procedure for the simulation of

† This paper was recommended for publication in revised form by Associate Editor Kyung-Soo Yang

*Corresponding author. Tel.: + 82 2 300 0285, Fax.: +82 2 3158 4429
E-mail address: mskim@kau.ac.kr

transient incompressible fluid flows using triangular meshes. His algorithm employed an artificial compressibility technique in connection with a dual time-stepping approach. Two-dimensional unsteady incompressible Navier-Stokes equations in vorticity-stream function formulation implemented a higher-order immersed boundary to solve unsteady incompressible flow by Linnick and Fasel[5].

It would be very valuable to study the flows past elliptic cylinders because engineering applications often involve flows over complex bodies like wings, submarines, missiles, and rotor blades, which can hardly be modeled as a flow over a circular cylinder. In such flows, cylinder thickness and angle of attack can greatly influence the nature of separation and the wake structure[6].

In 1987, Ota et al.[7] investigated the flow around an elliptic cylinder of axis ratio 1:3 in the critical Reynolds number regime, which extends from about Re =85,000 to 312,000, on the basis of mean static pressure measurements along the cylinder surface and of hot-wire velocity measurements in the near wake. Nair and Sengupta[8] solved Navier-Stokes equations in order to study the onset of computed asymmetry around elliptic cylinders at a Reynolds number of 10,000. They found that the ellipses developed asymmetry much earlier than did the circular cylinder. Kim and Sengupta[9] studied unsteady flow past an elliptic cylinder whose axis ratios are 0.6, 0.8, 1.0, and 1.2 at different Reynolds numbers of 200, 400, and 1,000 to investigate the unsteady lift and drag forces. They found that the elliptic cylinder thickness and Reynolds number could affect significantly the frequencies of the force oscillations as well as the mean values and the amplitudes of the drag and lift forces.

Many people also investigated the effect of incident angles. Patel[10] investigated the incompressible viscous flow around an impulsively started elliptic cylinder at 0°, 30°, 45° and 90° incidences and at the Reynolds numbers of 100 and 200. He solved the system of coupled partial differential equations by substituting the expanded finite Fourier series of the stream and vorticity functions in the Navier-Stokes equations. Chou and Huang[11] proposed a semi-explicit finite difference scheme to study the unsteady two-dimensional incompressible flow past a blunt object at high Reynolds numbers up to 40,000. They considered the aspect ratio and angle of attack as controlled parameters. In 2001, Badr et al.[12] used a series truncation method based on Fourier series to reduce the Navier-Stokes equations. The Reynolds number range was up to 5,000 and axis ratios of the elliptic cylinder were between 0.5 and 0.6, and angle of attack ranges between 0° and 90°. They showed an unusual phenomenon of negative lift occurring shortly after the start of motion. Kim and Park[13] studied numerically to figure out the effects of elliptic cylinder thickness (thickness to chord ratios of 0.2, 0.4, and 0.6), angle of attack (10°, 20°, and 30°), and Reynolds number (400 and 600) on the unsteady lift and drag forces exerted on the elliptic cylinder. Through this study, they observed that the elliptic cylinder thickness, angle of attack, and Reynolds number are very important parameters for determining the unsteady characteristics of lift and drag forces.

Since many engineering structures have rectangular-shaped cross sections, many researchers have done unsteady flow investigations around rectangular cylinders experimentally or numerically in view of Reynolds number, angle of attack, and blockage ratio effects. Davis and Moore[14] solved two-dimensional incompressible Navier-Stokes equations to investigate the vortex-shedding phenomenon around a rectangle at the Reynolds numbers of 100 to 2800 with different angle of attacks and rectangle dimensions. They found that the properties of vortices, lift, drag, and Strouhal number are strongly dependent on the Reynolds numbers. Okajima[15] experimentally investigated vortex-shedding frequencies of various rectangular cylinders in a wind tunnel and in a water tank. He found that there was a certain range of Reynolds number for the cylinders with the width-to-height ratios of two and three where the flow pattern abruptly changed with a sudden discontinuity in Strouhal number. In 1993, Norberg[16] measured the pressure distributions along a rectangular cylinder's surface at angle of attack 0° to 90° with side ratios of 1.0, 1.62, 2.5, and 3.0. He also obtained Strouhal numbers using a hot-wire in the near-wake regions. He found that the flow showed a large influence of both angle of attack and side ratio due to reattachment and shear layer/edge interactions. Sohankar et al.[17] calculated unsteady 2-D flow around a square cylinder at incidence between 0° to 45° and Reynolds numbers of 45 to 200. They used a SIMPLEC algorithm with a non-staggered grid arrangement. They found that the onset of vortex shedding occurred within the interval $40 < \mathrm{Re} < 55$, with a decrease in Reynolds number with increasing angle of attack. In

1999, Sohankar et al.[18] also simulated two- and three-dimensional flow simulations around a square cylinder at the Reynolds numbers of 150 to 500 with a blockage ratio of 5.6%. The simulations indicated a transition from 2-D to 3-D shedding flow between Reynolds number of 150 and 200. The confined flow around a square cylinder mounted inside a plane channel was numerically investigated by using two different numerical techniques called lattice-Boltzmann automata and finite volume method by Breuer et al.[19]. The two different numerical techniques gave very close numerical solutions such as drag coefficient, recirculation length, and Strouhal number.

Most investigations of unsteady flow past blunt body have been accomplished for circular, elliptic, or rectangular cylinders. However, many engineering structures have complex geometric shapes rather than simple ones, for example, missiles, bullets, sea scan equipment, high-speed trains, or ships, etc. They have combined shapes of elliptic or rectangular geometry for its nose and base shapes.

The objective of the present research is to study the effects of geometric shapes and Reynolds numbers on the unsteady flow physics concentrating on the drag and lift forces exerted on the body. Unsteady viscous flows over four different shapes of blunt bodies such as circular cylinder, square cylinder, circular-nosed flat-based cylinder, and flat-nosed circular-based cylinder shown in Fig. 1 are simulated at different Reynolds numbers of 100, 200, 300, and 400 by solving the unsteady form of incompressible Navier-Stokes equations, which are written in two-dimensional body intrinsic orthogonal curvilinear coordinate system.

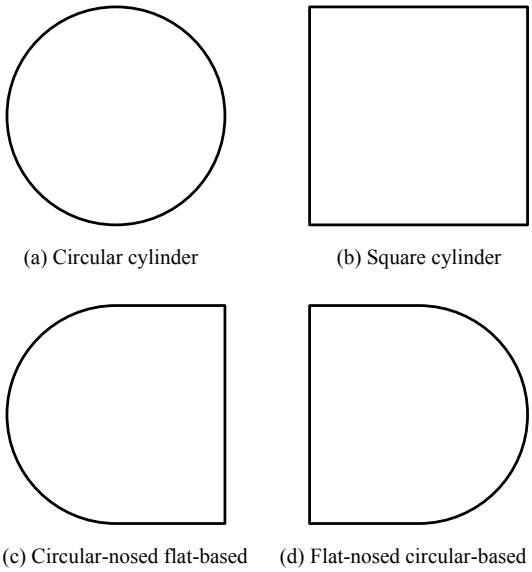

(a) Circular cylinder (b) Square cylinder

(c) Circular-nosed flat-based (d) Flat-nosed circular-based

Fig. 1. Two-dimensional cylinders.

For the temporal integration, the Crank-Nicolson scheme is used. Patankar[20] showed that the power law scheme ideally fits for all the Peclet numbers, so spatial discretization used this scheme. The discretized equations are solved by using a segregated approach where the discretized equation for each variable is solved sequentially using SIMPLER method.

2. Governing equations

2.1 Navier-Stokes equations

For the present analysis, the flowfield assumes two-dimensional unsteady, incompressible, laminar flow. The coordinate system is taken to be a two-dimensional, body-intrinsic, orthogonal curvilinear coordinate system as shown in Fig. 2 wherein the ξ-direction is taken to be along the body while the η-direction is perpendicular to the body surface. Here, $R(\xi)$ represents the radius of curvature at the point of ξ on the body surface. With these assumptions, continuity and momentum equations become as follows.

Continuity Equation:

$$\frac{\partial \rho}{\partial t}+\frac{1}{h_1}\frac{\partial}{\partial \xi}(\rho v_\xi)+\frac{1}{h_1}\frac{\partial}{\partial \eta}(h_1 \rho v_\eta)=0 \tag{1}$$

Here, h_1 is scale factor in the ξ-direction. The first term can drop for incompressible flow but it retains here for convenience.

v_ξ-Momentum Equation:

$$\frac{\partial}{\partial t}(\rho v_\xi)+\frac{1}{h_1}\frac{\partial}{\partial \xi}\left(\rho v_\xi v_\xi-\frac{1}{h_1}\mu\frac{\partial v_\xi}{\partial \xi}\right)+\frac{1}{h_1}\frac{\partial}{\partial \eta}\left(h_1\rho v_\eta v_\xi-h_1\mu\frac{\partial v_\xi}{\partial \eta}\right)$$
$$=-\frac{1}{h_1}(\rho v_\xi v_\eta)\frac{\partial h_1}{\partial \eta}-\frac{1}{h_1}\frac{\partial p}{\partial \xi}+\frac{\mu}{h_1}\left[\frac{\partial}{\partial \xi}\left(\frac{v_\eta}{h_1}\frac{\partial h_1}{\partial \eta}\right)+\left(\frac{1}{h_1}\frac{\partial v_\eta}{\partial \xi}-\frac{v_\xi}{h_1}\frac{\partial h_1}{\partial \eta}\right)\frac{\partial h_1}{\partial \eta}\right] \tag{2}$$

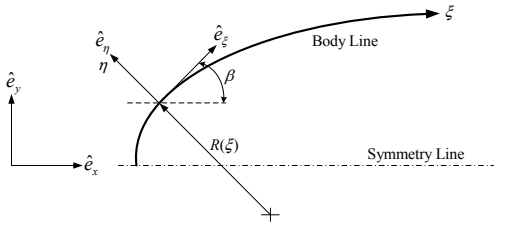

Fig. 2. Two-dimensional body-intrinsic coordinate system.

v_η -Momentum Equation:

$$\frac{\partial}{\partial t}(\rho v_\eta)+\frac{1}{h_1}\frac{\partial}{\partial \xi}\left(\rho v_\xi v_\eta-\frac{1}{h_1}\mu\frac{\partial v_\eta}{\partial \xi}\right)+\frac{1}{h_1}\frac{\partial}{\partial \eta}\left(h_1\rho v_\eta v_\eta-h_1\mu\frac{\partial v_\eta}{\partial \eta}\right)$$
$$=-\frac{1}{h_1}(\rho v_\xi v_\xi)\frac{\partial h_1}{\partial \eta}-\frac{\partial p}{\partial \eta}+\frac{\mu}{h_1}\left[\frac{\partial}{\partial \xi}\left(\frac{v_\xi}{h_1}\frac{\partial h_1}{\partial \eta}\right)-\left(\frac{1}{h_1}\frac{\partial v_\xi}{\partial \xi}-\frac{v_\eta}{h_1}\frac{\partial h_1}{\partial \eta}\right)\frac{\partial h_1}{\partial \eta}\right] \tag{3}$$

2.2 Discretization of governing equations

The surface and time integration of the governing equations over the control volume can be done term by term and expressed as follows in the intrinsic curvilinear coordinate system. All the detailed derivations of the following discretized governing equations can be found in Senguta[21].

Continuity Equation:

$$(\rho-\rho^0)\frac{h_1\Delta\xi\Delta\eta}{\Delta t}+\alpha(F_{i+\frac{1}{2},j}-F_{i-\frac{1}{2},j}+F_{i,j+\frac{1}{2}}-F_{i,j-\frac{1}{2}})$$
$$+(1-\alpha)(F^0_{i+\frac{1}{2},j}-F^0_{i-\frac{1}{2},j}+F^0_{i,j+\frac{1}{2}}-F^0_{i,j-\frac{1}{2}})=0 \tag{4}$$

where

$$F_{i+\frac{1}{2},j}=(\rho v_\xi)_{i+\frac{1}{2},j}\Delta\eta\,,\quad F_{i-\frac{1}{2},j}=(\rho v_\xi)_{i-\frac{1}{2},j}\Delta\eta\,,$$
$$F_{i,j+\frac{1}{2}}=(h_1\rho v_\eta)_{i,j+\frac{1}{2}}\Delta\xi\,,\quad F_{i,j-\frac{1}{2}j}=(h_1\rho v_\eta)_{i,j-\frac{1}{2}j}\Delta\xi$$

Here, superscript "0" represents the variable quantity at the old time step.

v_ξ -Momentum Equation:

$$[(\rho v_\xi)-(\rho v_\xi)^0]\frac{h_1\Delta\xi\Delta\eta}{\Delta t}+\alpha\left(J_{v_{\xi_{i+\frac{1}{2},j}}}-J_{v_{\xi_{i-\frac{1}{2},j}}}+J_{v_{\xi_{i,j+\frac{1}{2}}}}-J_{v_{\xi_{i,j-\frac{1}{2}}}}\right)$$
$$+(1-\alpha)\left(J^0_{v_{\xi_{i+\frac{1}{2},j}}}-J^0_{v_{\xi_{i-\frac{1}{2},j}}}+J^0_{v_{\xi_{i,j+\frac{1}{2}}}}-J^0_{v_{\xi_{i,j-\frac{1}{2}}}}\right) \tag{5}$$
$$=\left(\alpha S_{v_\xi}+(1-\alpha)S^0_{v_\xi}\right)_{i,j}h_1\Delta\xi\Delta\eta+(p_{i-1,j}-p_{i,j})\Delta\eta$$

where

$$J_{v_\xi\xi}=\left(\rho v_\xi v_\xi-\frac{1}{h_1}\mu\frac{\partial v_\xi}{\partial \xi}\right)\Delta\eta\,,\quad J_{v_\xi\eta}=\left(h_1\rho v_\xi v_\eta-h_1\mu\frac{\partial v_\xi}{\partial \eta}\right)\Delta\xi$$
$$S_{v_\xi}=-\frac{1}{h_1}(\rho v_\xi v_\eta)\frac{\partial h_1}{\partial \eta}+\frac{\mu}{h_1}\left[\frac{\partial}{\partial \xi}\left(\frac{v_\eta}{h_1}\frac{\partial h_1}{\partial \eta}\right)+\left(\frac{1}{h_1}\frac{\partial v_\eta}{\partial \xi}-\frac{v_\xi}{h_1}\frac{\partial h_1}{\partial \eta}\right)\frac{\partial h_1}{\partial \eta}\right]$$

v_η -Momentum Equation:

$$[(\rho v_\eta)-(\rho v_\eta)^0]\frac{h_1\Delta\xi\Delta\eta}{\Delta t}+\alpha\left(J_{v_{\eta_{i+\frac{1}{2},j}}}-J_{v_{\eta_{i-\frac{1}{2},j}}}+J_{v_{\eta_{i,j+\frac{1}{2}}}}-J_{v_{\eta_{i,j-\frac{1}{2}}}}\right)$$
$$+(1-\alpha)\left(J^0_{v_{\eta_{i+\frac{1}{2},j}}}-J^0_{v_{\eta_{i-\frac{1}{2},j}}}+J^0_{v_{\eta_{i,j+\frac{1}{2}}}}-J^0_{v_{\eta_{i,j-\frac{1}{2}}}}\right) \tag{6}$$
$$=\left(\alpha S_{v_\eta}+(1-\alpha)S^0_{v_\eta}\right)_{i,j}h_1\Delta\xi\Delta\eta+(p_{i,j-1}-p_{i,j})h_1\Delta\xi$$

where

$$J_{v_\eta\xi}=\left(\rho v_\eta v_\xi-\frac{1}{h_1}\mu\frac{\partial v_\xi}{\partial \xi}\right)\Delta\eta\,,\quad J_{v_\eta\eta}=\left(h_1\rho v_\eta v_\eta-h_1\mu\frac{\partial v_\eta}{\partial \eta}\right)\Delta\xi$$
$$S_{v_\eta}=-\frac{1}{h_1}(\rho v_\xi v_\xi)\frac{\partial h_1}{\partial \eta}+\frac{\mu}{h_1}\left[\frac{\partial}{\partial \xi}\left(\frac{v_\xi}{h_1}\frac{\partial h_1}{\partial \eta}\right)-\left(\frac{1}{h_1}\frac{\partial v_\xi}{\partial \xi}-\frac{v_\eta}{h_1}\frac{\partial h_1}{\partial \eta}\right)\frac{\partial h_1}{\partial \eta}\right]$$

3. Flow solver development

The solution algorithm used in the present work employs the SIMPLER algorithm developed by Patankar[20] in conjunction with the time integration method such as Crank-Nicolson and fully implicit.

3.1 Pressure equation

In the SIMPLER algorithm, the pressure equation comes out by manipulating the discretized continuity and momentum equations, and the pressure field is calculated by using this pressure equation with guessed velocity field.

Equation (7) shows the pressure equation over a control volume in the intrinsic curvilinear coordinate system. Its derivation and description of the coefficients are omitted here and Sengupta[21] explains them in detail.

$$a_{i,j}p^{"}_{i,j}=a_{i+1,j}p^{"}_{i+1,j}+a_{i-1,j}p^{"}_{i-1,j}+a_{i,j+1}p^{"}_{i,j+1}+a_{i,j-1}p^{"}_{i,j-1}-b_{i,j} \tag{7}$$

3.2 Pressure-correction equation

The pressure correction field, P', which is obtained by solving the pressure-correction equation (Equation 8) such that the continuity equation is satisfied, is used to update the imperfect velocity field obtained from solving the momentum equations.

$$a_{i,j}p^{'}_{i,j}=a_{i+1,j}p^{'}_{i+1,j}+a_{i-1,j}p^{'}_{i-1,j}+a_{i,j+1}p^{'}_{i,j+1}+a_{i,j-1}p^{'}_{i,j-1}-b_{i,j} \tag{8}$$

Since the derivation of the equations and the description of the whole structure of the calculation procedure for SIMPLER algorithm are not the main issues here, all of these are omitted in this paper, and Patankar[20] describes these more in detail.

3.3 Solution of the Algebraic equations

In the present work, a segregated approach is used to solve the discretized equations where each of the governing equations is solved sequentially. In each time step, the tri-diagonal matrix algorithm (TDMA) solves the simultaneous algebraic equations resulting in a tri-diagonal system for the entire grid mesh. Alternate ξ and η sweeps in the computational plane are performed to improve the overall convergence history even though absolute convergence is not required in each time step. One advances to the next time step when a sufficient converged criterion is satisfied. An under-relaxation is generally required between each TDMA update to prevent the solution from diverging.

3.4 Computational domain and solution verification

The flow geometry along with the boundary conditions and grid structure is shown in Fig. 3. The outer boundary of the computational domain has 50 times of unit-chord-length distance from the center of the blunt body. Here, the chord is defined as a straight line connecting the leading edge and trailing edge of the body. A no-slip boundary condition applies to the solid wall surface and free stream conditions apply to the inflow and outflow boundary conditions. The cyclic boundary condition is also implemented to see the unsteady flow physics. The O-mesh shaped 198x100 grid is generated algebraically.

Since most studies for unsteady flow past a blunt body have been performed for a circular cylinder, the verification of flow solver is carried out by comparing the present numerical solutions with currently available numerical and experimental data for a flow past a circular cylinder. Table 1 summarizes this comparison result and shows a good agreement in general.

Table 1. Comparison of the present results with available numerical / experimental data.

Re	Contributor	*St*	$\overline{Cd}$	ΔCd	ΔCl	$\overline{Cpb}$	ΔCpb
100	Present	0.13	1.28	0.01	0.43	-0.69	0.03
	Jordan,Fromm[2]	0.16	1.28	0.01	0.27	-0.66	0.02
	Acrivos*‡					-0.60	
200	Present	0.15	1.24	0.04	0.76	-0.88	0.14
	Rogers, Kwak†	0.18	1.23	0.05	0.65		
	Belov†	0.19	1.19	0.04	0.64		
	Linnick,Fasel[5]	0.19	1.34	0.04	0.69		
	Berger*[22]	0.18					
300	Present	0.16	1.23	0.06	0.92	-1.00	0.21
	Roshko*‡	0.20					
	Wieselsberger*‡		1.20				
400	Present	0.16	1.23	0.08	1.00	-1.07	0.26
	Jordan,Fromm[2]	0.20	1.23	0.07	0.75	-1.01	0.16
	Gerrard*‡					-0.85	

Note: 1. (*) denotes experimental data
2. (†) in Linnick and Fasel [5]
3. (‡) in Jordan and Fromm [2]

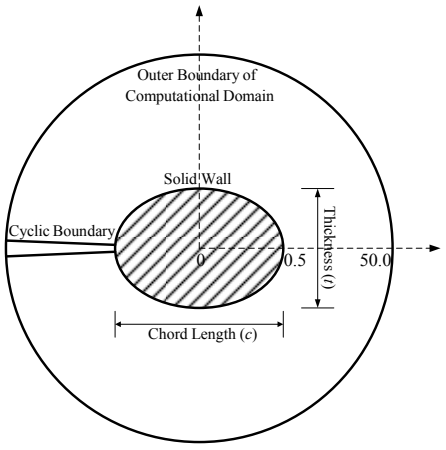

(a) Flow geometry and computational domain

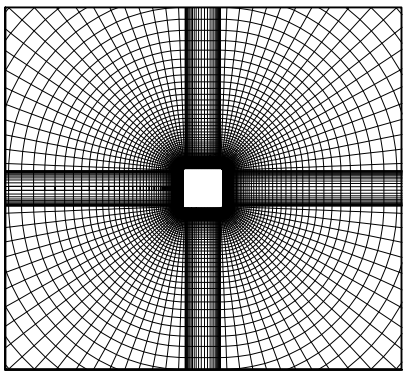

(b) Square grid (198x100)

Fig. 3. Computational domain and grid structure.

4. Numerical results and discussions

Vortex shedding that occurs alternately behind a blunt body generates a periodic and asymmetric flow pattern, and this flow pattern makes the periodic force. The periodic force acts on the blunt body in the free stream direction as drag force and normal direction to the free stream as lift force. The drag and lift forces exerted on the body can be decomposed into pressure force and friction force components as follows:

$$Cd = Cdp + Cdf\ , \qquad Cl = Clp + Clf$$

Here, Cdp and Cdf are the pressure and friction components of the drag coefficient, and Clp and Clf are the pressure and friction components of the lift coefficient, respectively.

Fig. 4 shows typical time variations of Cl and Cd as a function of non-dimensional time T for the circular cylinder at Re =200. Here, the lift and drag coefficients, Cl and Cd, are defined, respectively, as $Cl = 2L/(\rho\, U_\infty^2 c)$ and $Cd = 2D/(\rho U_\infty^2 c)$, where ρ, U_∞, L, D, and c are the fluid density, free-stream velocity, lift force per unit span, drag force per unit span, and the cylinder chord length, respectively. Also, the dimensionless time T is defined as $T = \dfrac{t}{c/U_\infty}$, where t is dimensional time. In this figure, oscillating frequencies and amplitudes of both coefficients can be compared very clearly. The amplitude of Cl is much greater than that of Cd, and the frequency of Cl is one-half the frequency of Cd. The frequency of Cl due to the vortex shedding can be expressed as the Strouhal number, which is non-dimensional parameter defined as follows.

$$St = \frac{f \times c}{U_\infty}$$

where f is the frequency of lift force oscillation. In addition, Fig. 4 shows that the amplitudes of friction force oscillations are much less than those of pressure force oscillations for both drag and lift forces.

Figs. 5 and 6 plot the streamline patterns and vortex shedding shapes behind the four different shapes of cylinders at the maximum lift condition, respectively, which means when the vortex shedding occurs at the bottom surface. Even though the streamline patterns and vortex shedding shapes are very similar to each other, the sizes of wake regions are different. That means the location of separation point is different depending on the body shapes. The wake size becomes larger when the cylinder has a flat-based geometry rather than the circular-based one no matter what the nose shape is.

Fig. 7 shows the Strouhal number variation according to the variation of Reynolds number for the four different shapes of cylinders. In the caption box of the figure, "rec" designates a flat-nosed or flat-based shape of geometry and "cir" does a circular-nosed or circular-based shape of geometry. For example, "rec-cir" means flat-nosed circular-based shape of cylinder body as shown in Fig. 1(d).

The Strouhal number increases as the Reynolds number increases for the circular-nosed geometry shapes. On the other hand, in case of flat-nosed geometry shapes, the Strouhal number increases as the

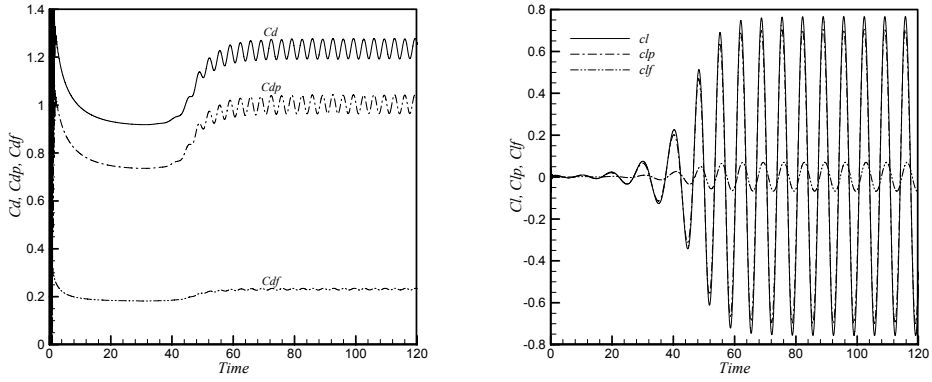

(a) Drag coefficient (b) Lift coefficient

Fig. 4. Time variations of drag and lift coefficients for circular cylinder at Re =200.

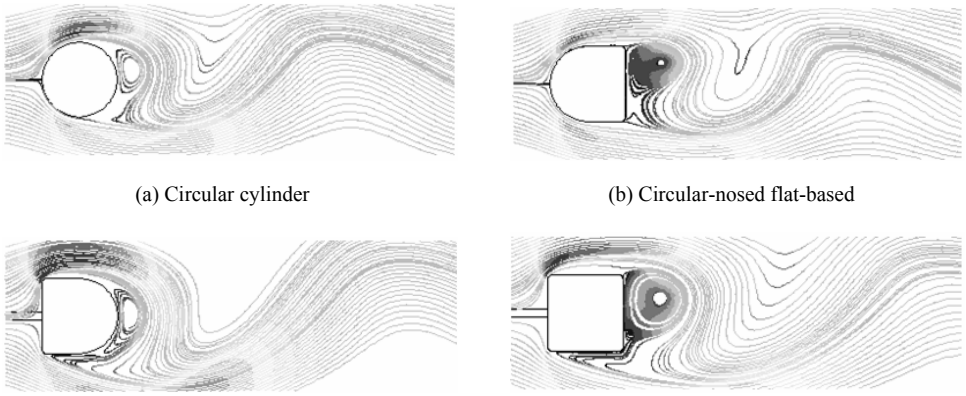

(a) Circular cylinder (b) Circular-nosed flat-based

(c) Flat-nosed circular-based (d) Square cylinder

Fig. 5. Streamline patterns at the maximum lift condition (*Re* =400).

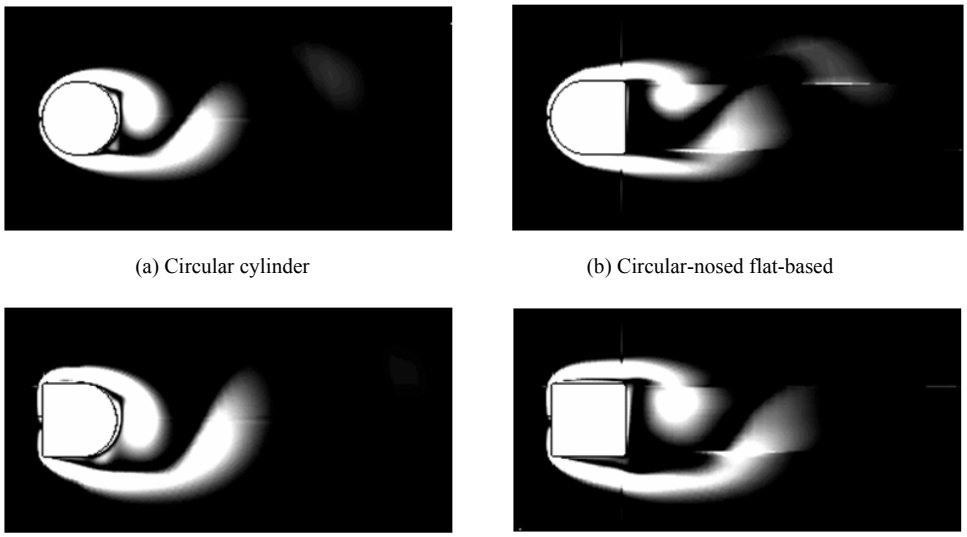

(a) Circular cylinder (b) Circular-nosed flat-based

(c) Flat-nosed circular-based (d) Square cylinder

Fig. 6. Vortex shedding at the maximum lift condition (*Re* =400).

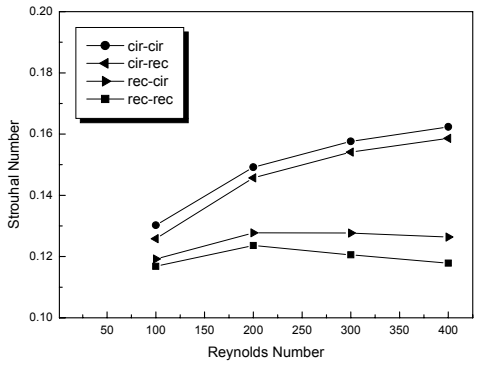

Fig. 7. Strouhal number versus Reynolds number.

Reynolds number increases up to a Reynolds number of 200, then it decreases as the Reynolds number increases. The pattern of the Strouhal number variation with Reynolds number is strongly dependent on the nose shape of the body.

A circular-nosed body has a higher oscillating frequency than a flat-nosed body because the flow separation behind a circular-nosed body occurs more easily than behind a flat-nosed body due to body surface curvature. In other words, the inertia force has more friction loss along the curved surface than flat surface and flow separates more easily from the body. In addition, a circular-based body has a little bit higher

oscillating frequency than a flat-based body due to easy flow separation coming from adverse pressure gradient along the curved body surface when the nose body shapes are the same. Namely, vortex shedding occurs more frequently when a body has circular shape rather than flat shape as shown in Fig. 7. Fig. 7 shows that a circular cylinder (cir-cir) has the highest oscillating frequency and a square cylinder (rec-rec) has the lowest oscillating frequency.

Fig. 8 shows the time-averaged total drag coefficient $\overline{Cd}$, time-averaged pressure drag coefficient $\overline{Cdp}$, and time-averaged friction drag coefficient $\overline{Cdf}$ versus Reynolds number. The magnitude of $\overline{Cd}$ is larger when the nose shape is flat no matter what the base shape is because high-pressure acts on the larger surface area in case of a flat-nosed body compared to circular-nosed body as shown in Fig. 9. Meanwhile, the magnitude of $\overline{Cdp}$ is larger when

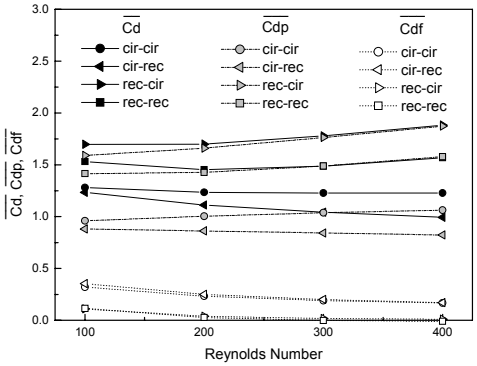

Fig. 8. $\overline{Cd}$, $\overline{Cdp}$, and $\overline{Cdf}$ versus Reynolds number

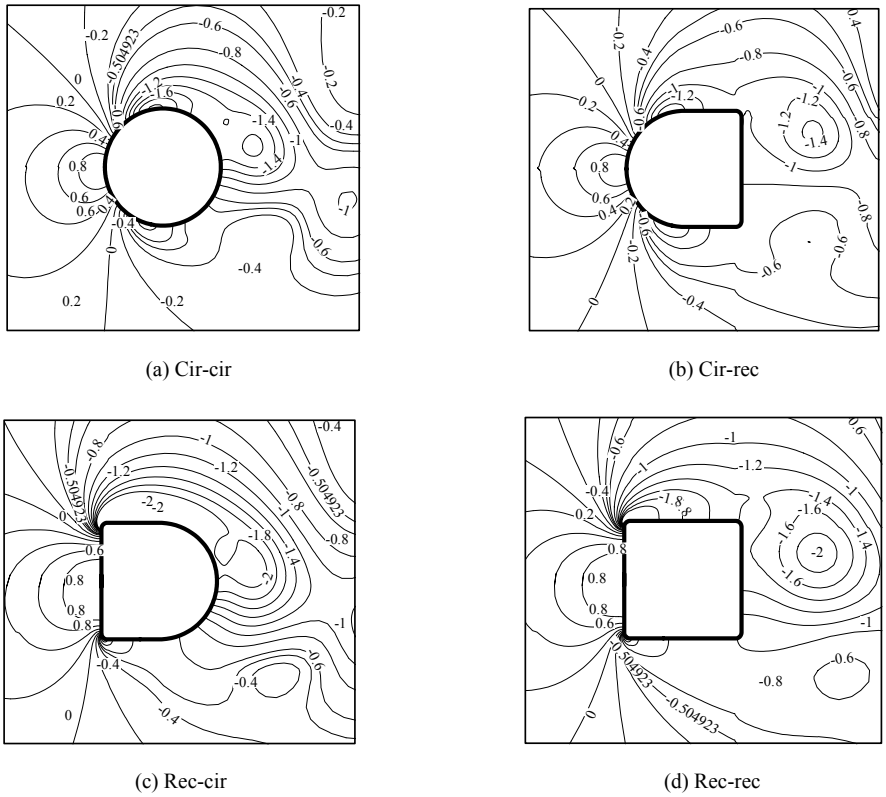

(a) Cir-cir (b) Cir-rec

(c) Rec-cir (d) Rec-rec

Fig. 9. Pressure contours at the maximum drag condition ($Re = 400$).

the base shape is circular than if the base shape is flat if they have the same nose shapes because the flow accelerates along the curved surface; therefore, the pressure becomes lower, which means the lower-pressure area in the base region becomes larger as shown in Fig. 9. For these reasons, the flat-nosed circular-based geometry has the maximum $\overline{Cdp}$ and circular-nosed flat-based geometry has the minimum $\overline{Cdp}$ among the four different geometries.

A circular-nosed geometry has larger $\overline{Cdf}$ compared to a flat-nosed geometry because shear force becomes large due to the high velocity gradient along the curved body surface. The geometric shape of base hardly affects the magnitude of $\overline{Cdf}$ because there is a re-circulating zone in that region. Fig. 10 complements these descriptions again. Here, the arc-length means the non-dimensional distance from a leading edge, which takes the chord length as a reference value, and negative $\overline{Cdf}$ on the lower surface represents that the friction force acts to the free-stream direction.

Most of the total drag comes from the pressure drag, and therefore a circular-nosed body shape is preferred to reduce the total drag force, whereas a flat-nosed body is preferred to reduce the friction drag force.

The time-averaged total drag coefficient $\overline{Cd}$ decreases as the Reynolds number increases up to 200 for all the geometries. As the Reynolds number in-

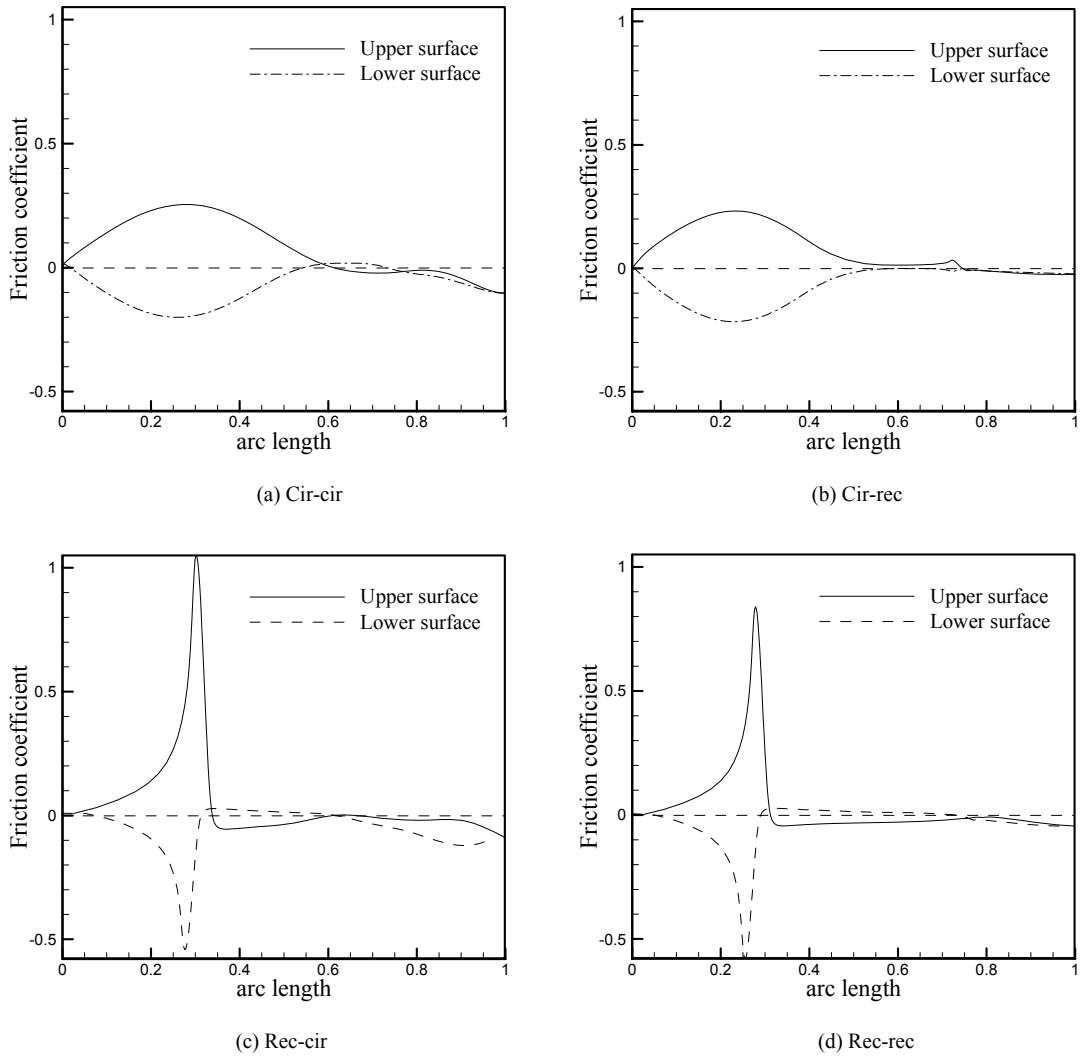

(a) Cir-cir

(b) Cir-rec

(c) Rec-cir

(d) Rec-rec

Fig. 10. Friction drag distributions along the body surface at the maximum drag condition ($Re = 400$).

creases more, $\overline{Cd}$ becomes larger when the geometry has flat-nosed shape, whereas $\overline{Cd}$ becomes smaller when the geometry has circular-nosed shape. On the other hand, $\overline{Cdf}$ decreases as the Reynolds number increases for all the shapes of bodies.

The amplitudes of lift and drag force oscillations are one of the very important physics in unsteady flow problems. At the beginning of this section, we mentioned that the amplitude of Cl is much greater than that of Cd . Here, the amplitudes of Cl and Cd oscillations are defined, respectively, as

$$\Delta Cl = \frac{(Cl)_{\max} - (Cl)_{\min}}{2} \qquad \Delta Cd = \frac{(Cd)_{\max} - (Cd)_{\min}}{2}$$

where the subscripts min and max denote the minimum and the maximum values, respectively, in a period.

Fig. 11 plots the variation of total drag coefficient oscillating amplitude ΔCd , pressure drag coefficient oscillating amplitude ΔCdp , and friction drag coefficient oscillating amplitude ΔCdf with Reynolds numbers. Here, note that $\Delta Cd \neq \Delta Cdp + \Delta Cdf$ because the maximum ΔCdp and the maximum ΔCdf do not occur simultaneously.

The ΔCd increases almost linearly as Reynolds number increases for all the geometries. It is clear that $\Delta Cd \simeq \Delta Cdp$ because the total drag force mostly comes from the pressure drag force as mentioned already. Therefore, the tendency of ΔCdp variation with Reynolds number is very similar to that of ΔCd .

Figs. 8 and 11 indicate that the larger $\overline{Cdp}$ is, the larger ΔCd is at the same Reynolds number. However, it is not true for the case of friction drag force. It seems that the magnitude of $\overline{Cdp}$ is related very closely to the magnitude of ΔCd .

Fig. 12 shows the amplitude of lift coefficient oscillation ΔCl , amplitude of lift coefficient oscillation due to pressure ΔClp , and amplitude of lift coefficient oscillation due to skin friction ΔClf with Reynolds numbers for the four different body shapes. Both ΔCl and ΔClp increase almost linearly with Reynolds number when the nose shape has flat geometry. However, when the nose shape has circular geometry, the magnitude of amplitude looks almost constant from the Reynolds number of 200.

A circular cylinder has a little bit larger ΔCl and ΔClp than a square cylinder, unlike the case of drag force oscillation at the Reynolds numbers of 100, 200, and 300. However, flat-nosed circular-based or circular-nosed flat-based geometry has the same tendency

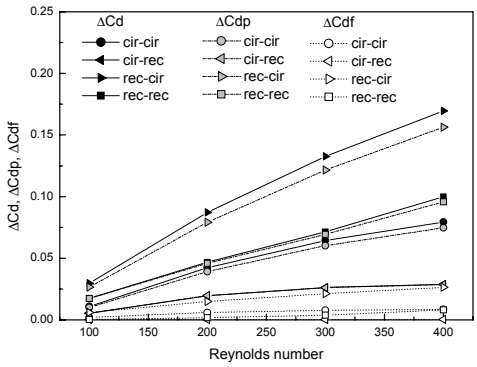

Fig. 11. ΔCd , ΔCdp , and ΔCdf versus Reynolds number.

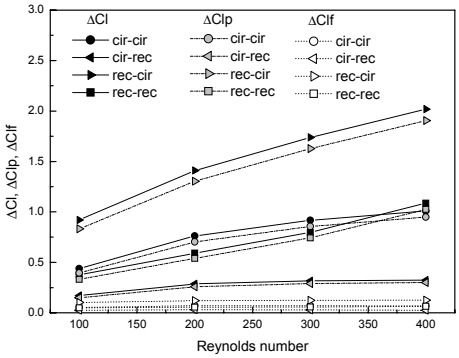

Fig. 12. ΔCl , ΔClp , and ΔClf versus Reynolds number.

as drag force oscillation. On the other hand, neither body shape nor Reynolds number affects friction lift force oscillation.

According to Figs. 12 and 13, it is found that the larger the pressure lift force is, the larger the lift force amplitude is at the same Reynolds number. Therefore, a flat-nosed circular-based cylinder has the maximum ΔCl and ΔClp , whereas a circular-nosed flat-based cylinder has the minimum ΔCl and ΔClp .

Fig. 14 plots base pressure coefficient $\overline{Cpb}$, which means pressure coefficient at the rear stagnation point, for the four different blunt bodies at different Reynolds numbers. Fig. 14 reconfirms Fig. 8, which compares $\overline{Cd}$ in a different way. The larger the $\overline{Cd}$ is, the smaller the $\overline{\mathrm{Cpb}}$ is.

Fig. 15 shows the variation of the base pressure oscillating amplitude ΔCpb with the variation of Reynolds numbers. The trend of amplitude variation with respect to Reynolds number and body shape is very similar to the trend of ΔCl as expected.

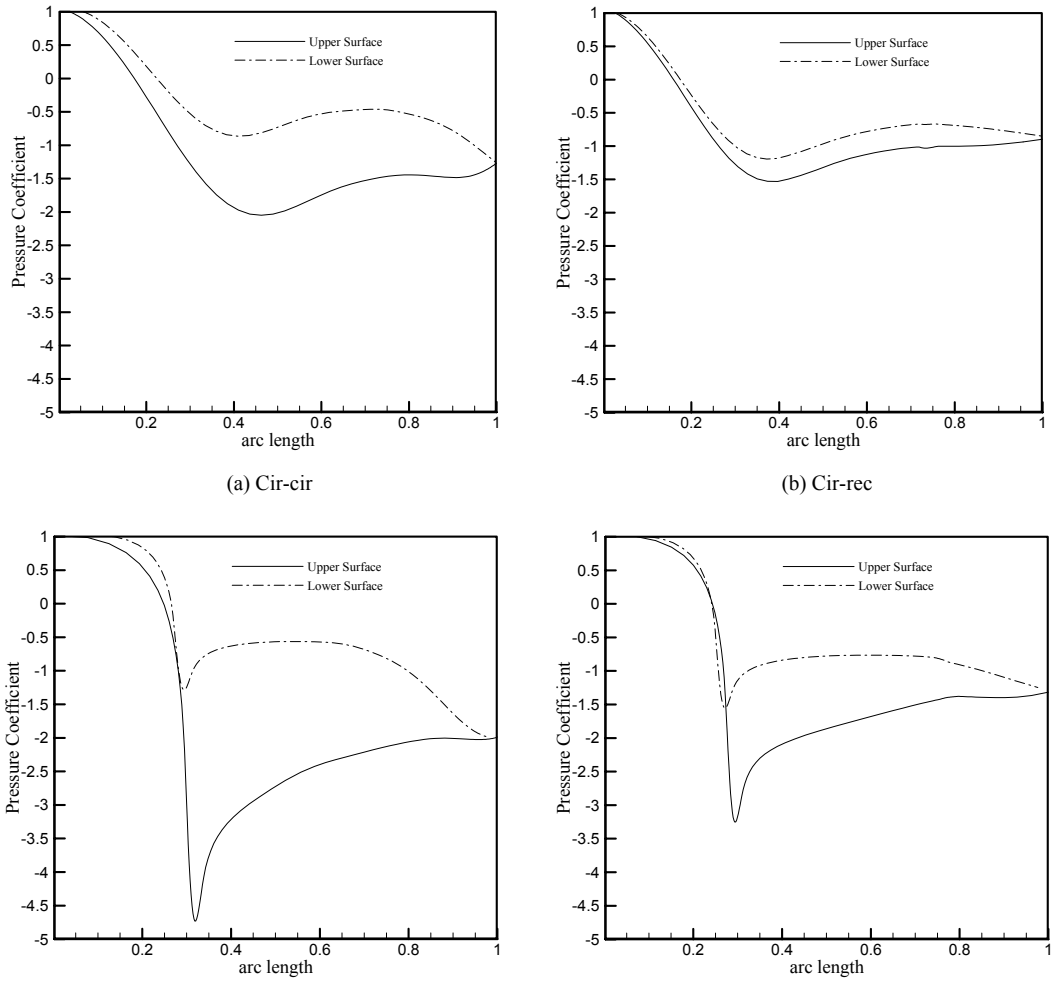

(a) Cir-cir (b) Cir-rec

(c) Rec-cir (d) Rec-rec

Fig. 13. Pressure distributions along the body surface at the maximum lift condition ($Re = 400$).

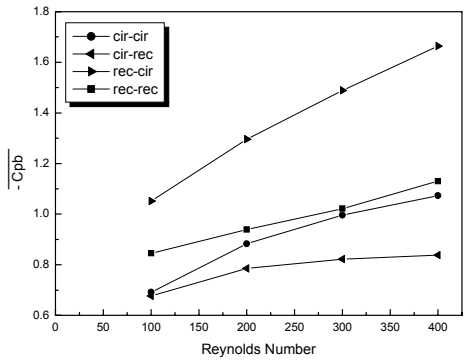

Fig. 14. $\overline{Cpb}$ versus Reynolds number

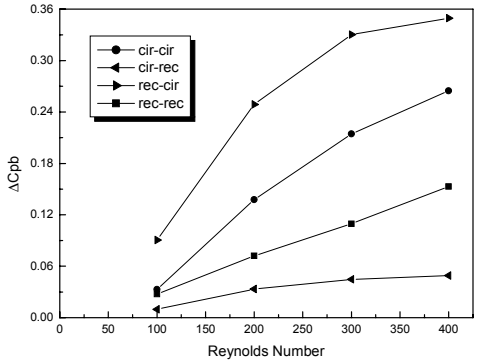

Fig. 15. ΔCpb versus Reynolds number.

5. Summary and conclusions

Through this study, we have investigated the effect of body shape and Reynolds number on the unsteady flow physics such as time-averaged drag coefficient, frequency of drag/lift coefficient oscillation, and the amplitude of oscillating drag/lift coefficient. The result is that the unsteady flow past a blunt body strongly depends on the blunt body shape and Reynolds number.

The nose shape of the blunt body is a key parameter for determining the tendency of frequency variation according to the variation of Reynolds number. A circular-nosed body oscillates more frequently as the Reynolds number increases, whereas a flat-nosed body oscillates less frequently. Besides, a circular-shaped body has higher oscillating frequency than a flat-shaped one at the same Reynolds number. Therefore, a circular cylinder has the largest Strouhal number, whereas a square cylinder has the smallest Strouhal number at the same Reynolds number.

Since most of the total drag force comes from the pressure drag, a circular-nosed body is a better choice for reducing the drag coefficient. In addition, a flat-based shape of the body is better than a circular-based shape of the body to reduce the drag coefficient. Therefore, a circular-nosed flat-based geometry is the best choice and a flat-nosed circular-based geometry is the worst choice from the viewpoint of drag force reduction. The friction drag coefficient is strongly dependent on the nose shape of the body only and decreases as Reynolds number increases. A circular-nosed body has larger friction drag coefficient than a flat-nosed body.

The magnitude of the drag/lift force strongly influences the amplitude of the oscillating drag/lift force. The larger the drag/lift coefficient is, the larger the amplitude of oscillating drag/lift coefficient is at the same Reynolds number. In addition, the amplitude of the oscillating drag/lift coefficient increases as Reynolds number increases for all the geometries.

Finally, we can have the following conclusions confined to the four different shapes of blunt bodies at moderate Reynolds numbers.

(1) A circular-nosed flat-based shape of geometry has the minimum drag coefficient and the minimum amplitude of oscillating drag/lift coefficient. In addition, this geometry has the maximum skin friction drag coefficient.

(2) A flat-nosed circular-based shape of geometry has the maximum drag coefficient and the maximum amplitude of oscillating drag/lift coefficient. In addition, it has the minimum skin friction drag coefficient.

(3) A circular cylinder has the highest oscillating frequency, whereas a square cylinder has the lowest oscillating frequency.

(4) The Strouhal number and force coefficient magnitude/amplitude are mutually incompatible. Namely, the Strouhal number is approximately in inverse proportion to the force coefficient magnitude/amplitude.

(5) The nose shape of the blunt body is a key parameter for determining the trend of Strouhal number variation with variation of Reynolds number, and the magnitude of friction drag coefficient strongly depends on the nose shape of the body at all Reynolds numbers.

References

[1] T. von Kármán, Uber den Mechanismus des Widerstandes den ein bewegter Korper in einer Flussigkeit Erfahrt, *Nachr. Ges. Wiss. Gottingen, Math-Phys Klasse*, 12 (1912) 509-517.

[2] S. K. Jordan and J. E. Fromm, Osicllatory Drag, Lift, and Torque on a Circular Cylinder in a Uniform Flow, *Physics of Fluids*, 15 (3) (1972) 371-376.

[3] H. M. Blackburn and R. D. Henderson, A Study of Two-Dimensional Flow Past an Oscillating Cylinder, *Journal of Fluid Mechanics*, 385 (1999) 255-286.

[4] M. T. Manzari, A Time-accurate Finite Element Algorithm for Incompressible Flow Problems, *International Journal of Numerical Methods for Heat & Fluid Flow*, 13 (2) (2003) 158-177.

[5] M. N. Linnick and H. F. Fasel, A High-Order Immersed Boundary Method for Unsteady Incompressible Flow Calculations, (2003) AIAA Paper 2003-1124.

[6] R. Mittal and S. Balachandar, Direct Numerical Simulation of Flow Past Elliptic Cylinders, *Journal of Computational Physics*, 124 (1996) 351-367.

[7] T. Ota, H. Nishiyama and Y. Taoka, Flow Around an Elliptic Cylinder in the Critical Reynolds Number Regime, *Journal of Fluids Engineering*, 109 (1987) 149-155.

[8] M. T. Nair and T. K. Sengupta, Onset of Asymmetry: Flow Past Circular and Elliptic Cylinders, *International Journal for Numerical Methods in Flu-*

ids, 23 (1996) 1327-1345.

[9] M. S. Kim and A. Sengupta, Unsteady Viscous Flow over Elliptic Cylinders at Various Thickness with Different Reynolds Numbers, *Journal of Mechanical Science and Technology*, 19 (3) (2005) 877-886.

[10] V. A. Patel, Flow Around the Impulsively Started Elliptic Cylinder at Various Angles of Attack, *Computers and Fluids*, 9 (4) (1981) 435-462.

[11] M. H. Chou and W. Huang, Numerical Study of High-Reynolds-Number Flow Past a Blunt Object, *International Journal for Numerical Methods in Fluids*, 23 (1996) 711-732.

[12] H. M. Badr, S. C. R. Dennis and S. Kocabiyik, Numerical Simulation of the Unsteady Flow Over an Elliptic Cylinder at Different Orientations, *International Journal for Numerical Methods in Fluids*, 37 (2001) 905-931.

[13] M. S. Kim and Y. B. Park, Unsteady Lift and Drag Forces Acting on the Elliptic Cylinder, *Journal of Mechanical Science and Technology*, 20 (1) (2006) 167-175.

[14] R. W. Davis and E. F. Moore, A numerical study of vortex shedding from rectangles, *Journal of Mechanics*, 116 (1982) 475-506.

[15] A. Okajima, Strouhal numbers of rectangular cylinders, *Journal of Fluid Mechanics*, 123 (1982) 379-398.

[16] C. Norberg, Flow around rectangular cylinders: Pressure forces and wake frequencies, *Journal of Wind Engineering and Industrial Aerodynamics*, 49 (1993) 187-196.

[17] A. Sohankar, C. Norberg and L. Davidson, Low-Reynolds-number flow around a square cylinder at incidence: study ofblockage, onset of vortex shedding and outlet boundary condition, *International Journal for Numerical Methods in Fluids*, 26 (1998) 39-56.

[18] A. Sohankar, C. Norberg and L. Davidson, Simulation of three-dimensional flow around a square cylinder at moderate Reynolds numbers, *Physics of Fluids*, 11 (2) (1999) 288-306.

[19] M. Breuer and J. Bernsdorf, T. Zeiser and F. Durst, Accurate computations of the laminar flow past a square cylinder based on two different methods: lattice-Boltzmann and finite-volume, *International Journal of Heat and Fluid Flow*, 21 (2000) 186-196.

[20] S. V. Patankar, *Numerical Heat Transfer and Fluid Flow*, Hemisphere, New York, USA, (1980).

[21] A. Sengupta, *Numerical Simulation of Unsteady Incompressible Flow Passed Two-Dimensional Elliptic Cylinders*, MS Thesis, Iowa State University, USA (2003).

[22] E. Berger and R. Wille, Periodic Flow Phenomena, *Ann. Rev. Fluid Mech*., 4 (1972) 313-340.

Moon-Sang Kim received his B.S. degree from Seoul National University Bachelor, M.S. in KAIST, and Ph.D. in Uni-versity of Illinois at Urbana-Champaign. He served at an engineer at Korea Power En-gineering Inc., and a Senior En-gineer at the Agency for Defense Development. He is currently a professor of Korea Aerospace University.